Supplement of Atmos. Chem. Phys., 26, 809–837, 2026
https://doi.org/10.5194/acp-26-809-2026-supplement

Atmospheric Chemistry and Physics
Open Access
EGU

Supplement of

Beyond binary maps from $HCHO/NO_2$: a deep neural network approach to global daily mapping of net ozone production rates and sensitivities constrained by satellite observations (2005–2023)

Amir H. Souri et al.

Correspondence to: Amir H. Souri (a.souri@nasa.gov)

Contents

S1. FNR is oblivious to impact of photolysis rates and water vapor content on PO_3 _____ 4

*S2. A Tale of Two Cities: Long-term trends of PO_3 in Los Angeles vs. Tehran in 2005-2019*__ 8

S3. Can rapid heatwaves accelerate PO_3 in the northeast U.S.? _____ 10

4. References: _____ 13

Figure S1. The PO_3 isopleths generated using F0AM box models derived from observations taken during the KORUS-AQ campaign under three different photolysis rates scenarios: (left) multiplied by 0.5, (middle) default, (right) multiplied by 2.0. Each contour represents 3 ppbv/hr. 4
Figure S2. The comparison of measured FNR and measured jNO_2 frequencies taken from aircraft observations during the KORUS-AQ campaigns. All measured points are used to make this plot. 5
Figure S3. Five variables derived from our PO_3DNN product based on TROPOMI dataset. The first row focuses on the December-January-February (DJF), while the second shows those variables for June-July-August 2023. The calculation of the sensitivities and derivatives are based on perturbation of the DNN algorithm described in the main paper. 6
Figure S4. The effect of H_2O(v) on PO_3 during KORUS-AQ campaigns. Only highly polluted regions ($HCHO \times NO_2 > 10$) are selected for this experiment. 7
Figure S5. The comparison of measured FNR and measured water vapor density taken from aircraft observations during the KORUS-AQ campaigns. All measured points are used to make this plot. 7
Figure S6. The statistically significant linear trends of PO_3 over LA (left) and Tehran (right) based on the PO_3DNN product in 2005-2019. 8
Figure S7. The statistically significant linear trends of PBL NO_2 mixing ratios over LA (left) and Tehran (right) based on the bias-corrected OMI and MINDS product in 2005-2019. 9
Figure S8. The maps of PO_3 within PBL in August 2007 (left), August 2008 (middle), and their absolute difference (right). 10
Figure S9. The maps of NO_2 (top) and HCHO (bottom) concentrations within PBL averaged in month of August in 2007 (heatwave) and 2008 (a normal condition), and their absolute differences. The abundance of HCHO and NO_2 are informed by bias-corrected OMI retrievals. 11
Figure S10. A similar layout as shown in Figure 8, but with the sensitivity outputs derived from the PO_3DNN algorithm. 12
Figure S11. The learning curve shows the evolution of training and validation MSEs as a function of epochs. 14
Figure S12. Scatterplots comparing observationally-constrained F0AM model PO_3 and the predictions based on the DNN for the whole data (test+validation+training) from each air quality campaign. "All" denotes all test data. 14
Figure S13. Scatterplots comparing observationally-constrained F0AM model PO_3 and the predictions based on dropping each campaign from the training data and using them as benchmarks. 15
Figure S14. Absolute values of HCHO, NO_2, and jNO_2 for several regions shown in Figure 7 in the main manuscript. These data are based on 2005-2007 time period. HCHO and NO_2 units are ppbv. jNO_2 is in 1×10^3/s unit. 16
Figure S15. Linear trends of HCHO mixing ratios within the PBL derived from OMI+MINDS in 2005-2019. Dots indicate a statistically significant trend. 17

Figure S16. Linear trends of NO_2 mixing ratios within the PBL derived from OMI+MINDS in 2005-2019. Dots indicate a statistically significant trend. 17
Figure S17. Recalculation of AMFs using MINDS vertical shape factors contrasted with the default profiles coming from TM5. The differences are within 20% in polluted regions with active photochemistry. 18
Figure S18. The impact of AMFs recalculation of TROPOMI NO_2 on relative PO_3 over regions undergoing PO_3>0.5 ppbv/hr. 18
Figure S19. Same as Figure S17 but for HCHO. 19
Figure S20. Same as Figure S18 but for HCHO. 19

S1. FNR is oblivious to impact of photolysis rates and water vapor content on PO_3

The primary objective of using the formaldehyde-to-nitrogen dioxide ratio (FNR) is to reduce high-dimensional, non-linear ozone production rates into a two-dimensional framework based on volatile organic compound reactivity (VOCR) and reactive nitrogen. However, beyond the fact that HCHO and NO_2 incompletely represent VOCR and reactive nitrogen, it is crucial to recognize that ozone production rate sensitivities and magnitudes depend on other geophysical variables independent of FNR. Among these variables, photolysis rates and water vapor are major drivers of atmospheric oxidation capacity, modulating numerous reactions related to ozone production (Kleinman et al., 2002).

To demonstrate photolysis rate effects on both PO_3 magnitudes and sensitivities, we conducted F0AM box model simulations constrained by geophysical variables during June 6-9 of the KORUS-AQ campaign (Souri et al., 2025). We perturbed NOx, VOCs, and photolysis rates to generate three sets of isopleths (Figure S1). The results clearly show larger ozone production rates under more intense light conditions. More importantly, the contours corresponding to identical PO_3 intervals (3 ppbv/hr) become more compact under brighter conditions, indicating that PO_3 becomes more sensitive to both NO_X and VOCs with increased light intensity. This pattern suggests that identical FNR values under different photolysis rates can have fundamentally different implications for ozone production rate sensitivities.

To confirm that FNR contains no photolysis rate information, we analyze paired FNR and jNO_2 photolysis rate measurements from over 47,000 data points during the KORUS-AQ campaign, revealing no correlation between these variables (Figure S2). This demonstrates the need for additional dimensions in ozone sensitivity analysis, necessitating more sophisticated algorithms (like our approach) over traditional threshold-based methods.

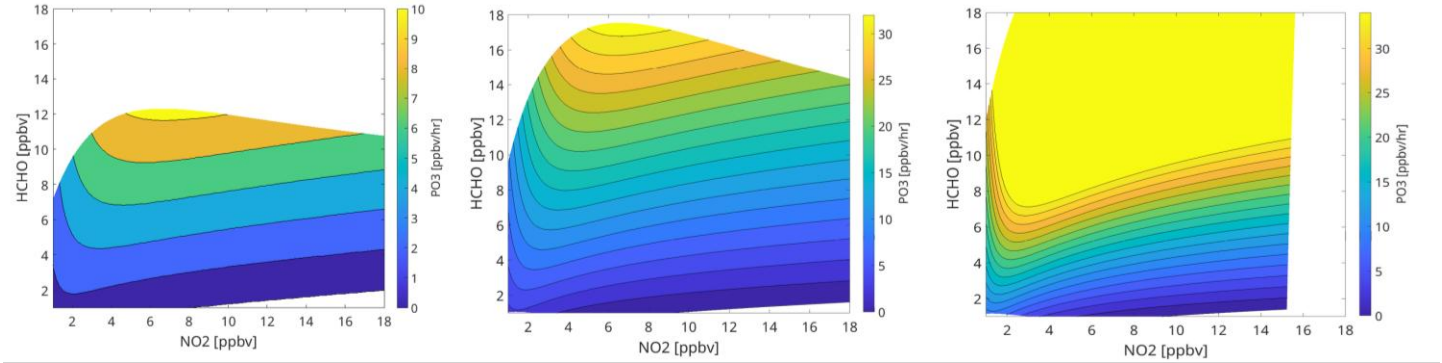

Figure S1. The PO_3 isopleths generated using F0AM box models derived from observations taken during the KORUS-AQ campaign under three different photolysis rates scenarios: (left) multiplied by 0.5, (middle) default, (right) multiplied by 2.0. Each contour represents 3 ppbv/hr.

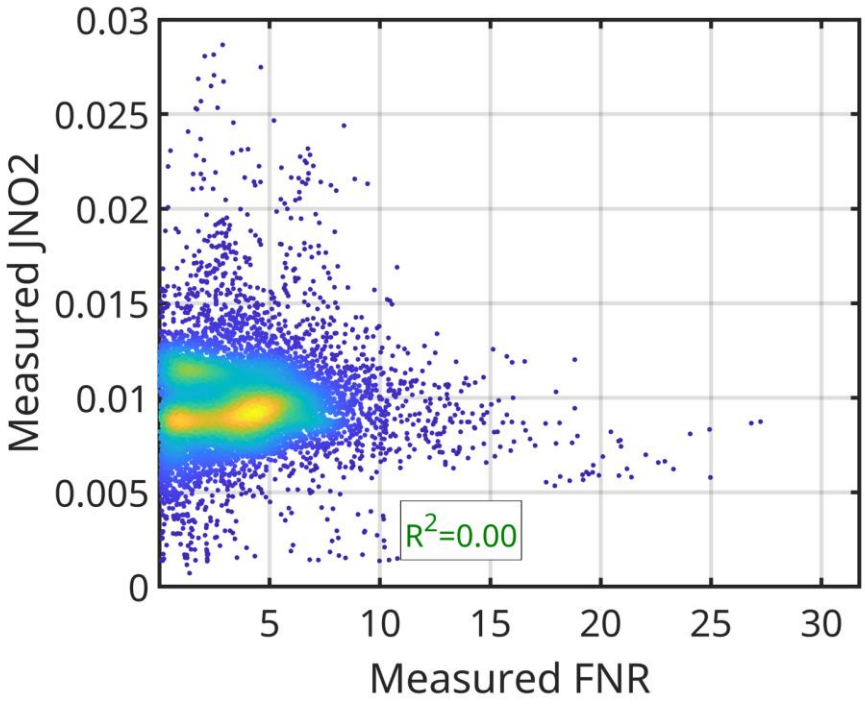

Figure S2. The comparison of measured FNR and measured jNO_2 frequencies taken from aircraft observations during the KORUS-AQ campaigns. All measured points are used to make this plot.

Figure S3 illustrates the incomplete representation of ozone sensitivities by mapping five variables derived from TROPOMI and our PO_3DNN parameterization across two seasons over Los Angeles. FNR values are low during colder months due to abundant NO_2 relative to HCHO, qualitatively suggesting the LA region should be predominantly VOC-sensitive. However, the derivatives and sensitivities of PO_3 to both HCHO and NO_2 remain muted due to limited photochemical activity, making PO_3 unresponsive to NO_X and VOC concentrations. Conversely, summer conditions yield larger derivatives, showing much stronger PO_3 responses to both species. This example extends to different times of day, such as FNR values from geostationary satellites or morning versus afternoon measurements from low Earth orbit satellites.

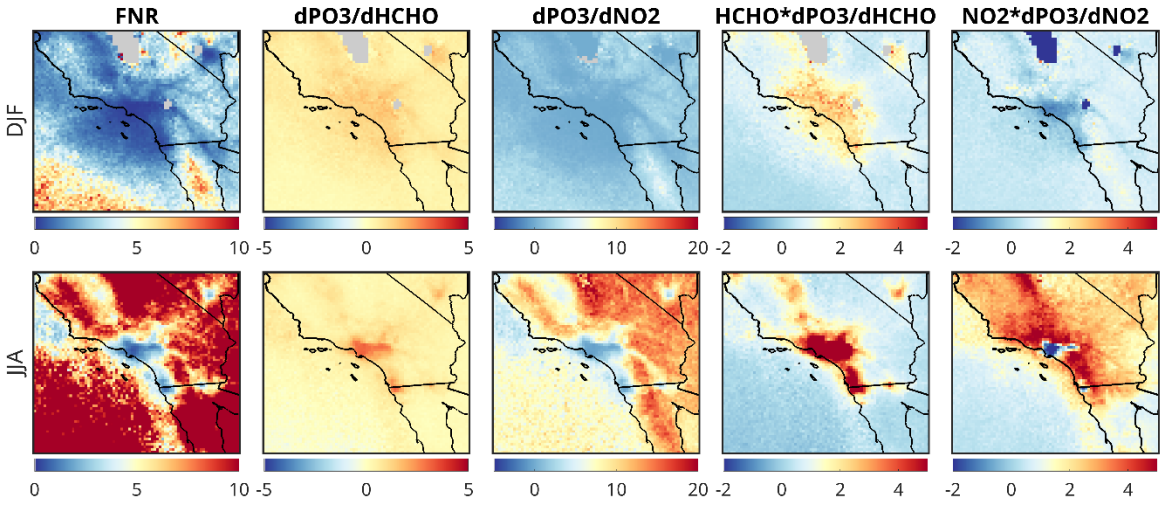

Figure S3. Five variables derived from our PO_3DNN product based on TROPOMI dataset. The first row focuses on the December-January-February (DJF), while the second shows those variables for June-July-August 2023. The calculation of the sensitivities and derivatives are based on perturbation of the DNN algorithm described in the main paper.

The absence of PO_3-relevant geophysical information in FNR also applies to water vapor. F0AM box simulations over polluted regions show that increasing humidity enhances PO_3 through the generation of two OH molecules via H_2O+O^1D reactions (Figure S4). However, FNR contains no water vapor information, as humidity is driven by hydrological and meteorological factors decoupled from the processes determining FNR (Figure S5). This further necessitates adding water vapor as an additional dimension in ozone sensitivity analysis.

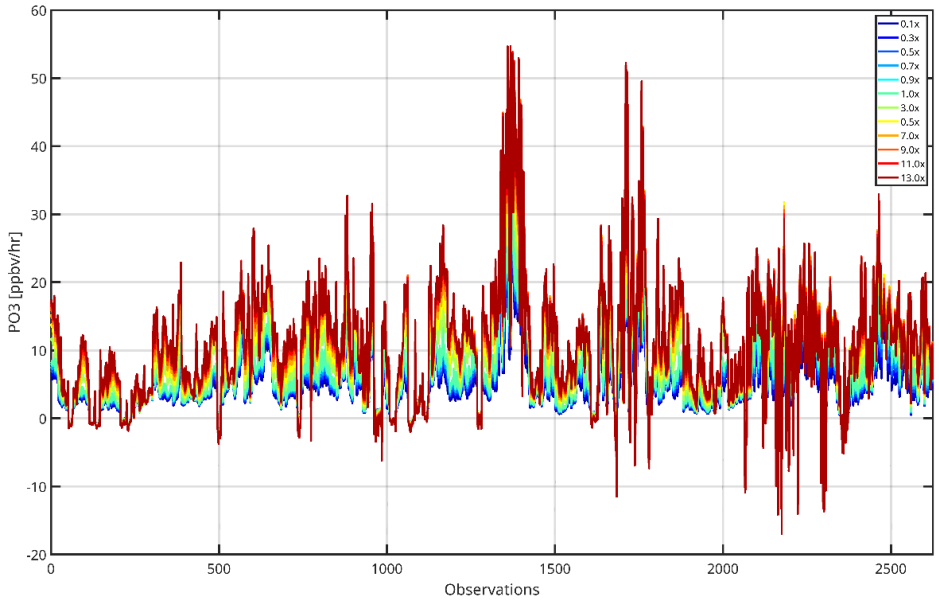

Figure S4. The effect of $H_2O(v)$ on PO_3 during KORUS-AQ campaigns. Only highly polluted regions ($HCHO \times NO_2 > 10$) are selected for this experiment.

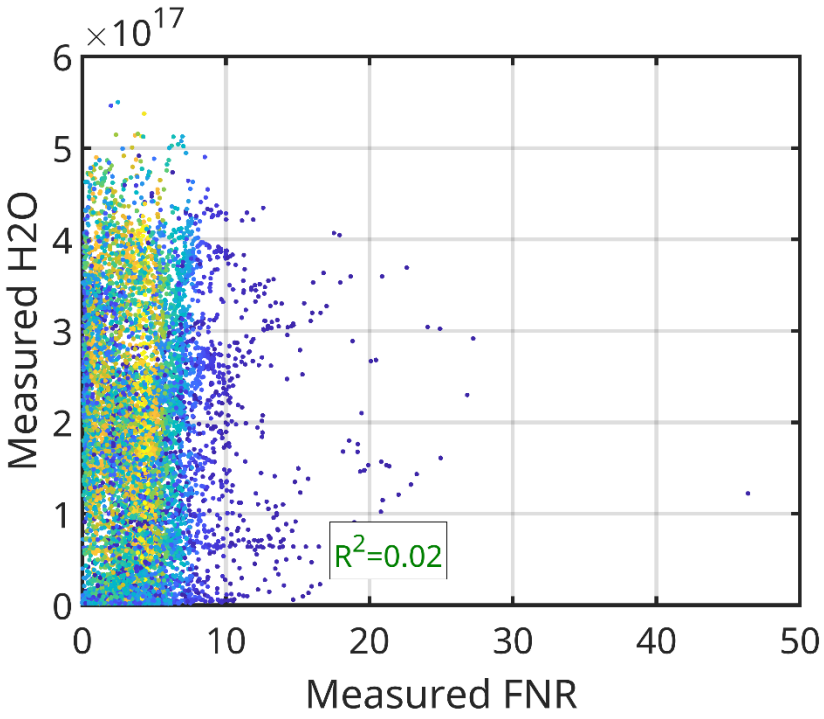

Figure S5. The comparison of measured FNR and measured water vapor density taken from aircraft observations during the KORUS-AQ campaigns. All measured points are used to make this plot.

S2. A Tale of Two Cities: Long-term trends of PO_3 in Los Angeles vs. Tehran in 2005-2019

Using a linear trend calculation method outlined by Souri et al. (2024), we evaluate the long-term linear trends of PO_3 maps in two cities: Los Angeles (USA) and Tehran (Iran). Figure S6 clearly demonstrates a complete reversal in the linear trends of PO_3, revealing an increase in Los Angeles and a decrease in Tehran. Moreover, we observe similar contrasting trends in the surrounding areas, with PO_3 levels rising near Tehran while declining near LA (Los Angeles). This tendency is a clear demonstration of non-linear ozone chemistry. While we do not identify any statistically significant trends in HCHO mixing ratios within the PBL for these two major cities, we do observe a significant downward trend in NO_2 mixing ratios in Los Angeles and a substantial upward trend in Tehran, as illustrated in Figure S7. Since both cities are primarily in VOC-sensitive conditions at their cores (Souri et al., 2025), it is intuitively clear a reduction (enhancement) in NO_2 should lead to positive (negative) trends in PO_3 because of the impact of the loss of NO_X on PO_3. Conversely, in their suburbs where the negative effect of the loss of NO_X on PO_3 diminishes, we see a close association of the sign of PO_3 trends and those of NO_2.

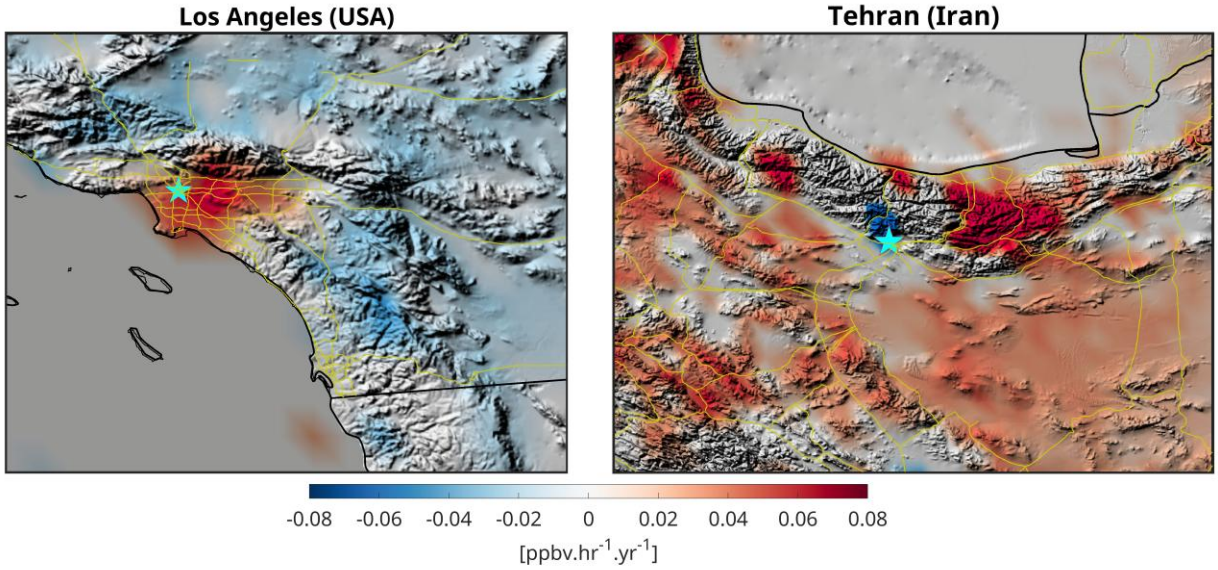

Figure S6. The statistically significant linear trends of PO_3 over LA (left) and Tehran (right) based on the PO_3DNN product in 2005-2019.

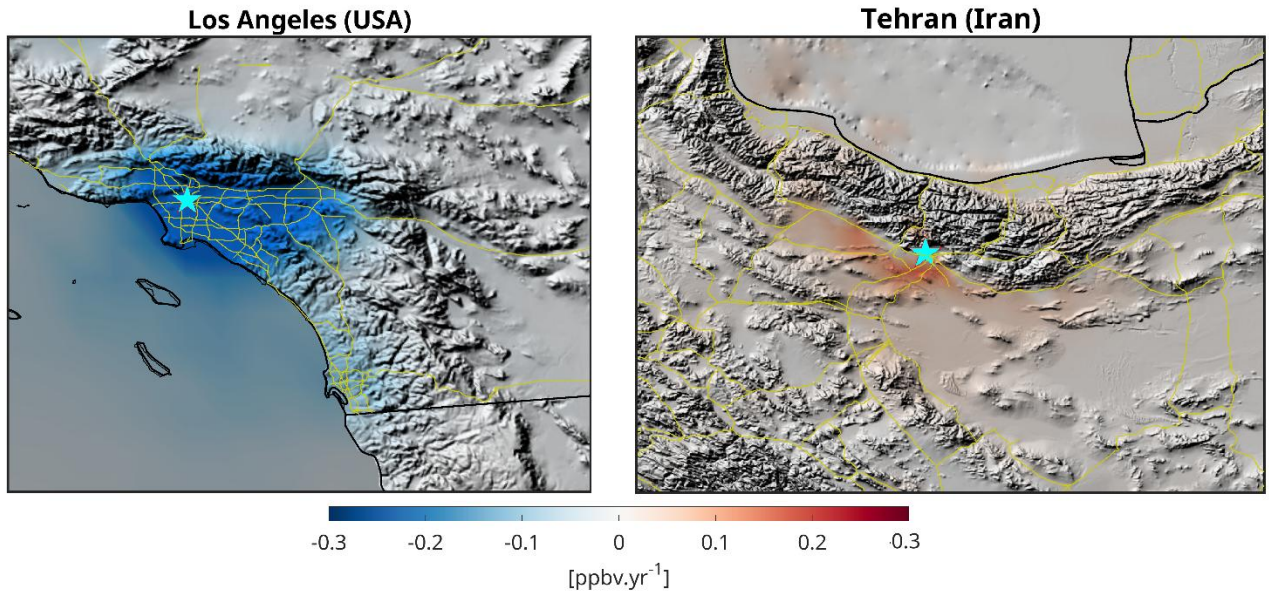

Figure S7. The statistically significant linear trends of PBL NO_2 mixing ratios over LA (left) and Tehran (right) based on the bias-corrected OMI and MINDS product in 2005-2019.

S3. Can rapid heatwaves accelerate PO_3 in the northeast U.S.?

Heatwaves are known to worsen ozone pollution in many regions because of several factors. Increased temperatures can elevate both anthropogenic and biogenic VOCs (Guenther et al., 2012; Wu et al., 2024). Additionally, higher temperatures can accelerate some key reaction rates, particularly NO+RO_2 (Pusede et al., 2015). Longer periods of active photochemistry can occur because of fewer clouds, and the dispersion of ozone and its precursors may be hindered by a dominant high-pressure system (Pyrgou et al., 2018). However, some of these effects may be offset if heatwaves last for an extended period, as drought conditions can suppress biogenic VOCs (Duncan et al., 2009; Demetillo et al., 2019). In this study, we focus on a severe heatwave that affected the eastern U.S. in August 2007. To contrast the atmospheric conditions during this month with those of a typical condition, we use August 2008 as a baseline.

Our PO_3DNN product shown in Figure S8 exhibits a 21% increase in PO_3 rates with respect to the baseline throughout the northeast U.S., suggesting that rapid heatwaves can accelerate the production of chemically-generated ozone molecules. It is important to acknowledge that both maps represent conditions with minimal cloud cover imposed by the cloud-screening flags from the satellite retrievals. However, the frequency of clear-sky conditions is usually higher during heatwaves compared to normal conditions. This distinction is critical because clouds play a significant role in reducing photochemical activity close to the surface by limiting incoming solar radiation. Consequently, even if PO_3 values appeared similar between these two episodes, the more frequent occurrence of clear-sky conditions in August 2007 would result in a greater cumulative contribution of PO_3 to the region. This highlights the impact of persistent sunshine in enhancing ozone, reinforcing the need to account for meteorological variability when analyzing photochemical processes.

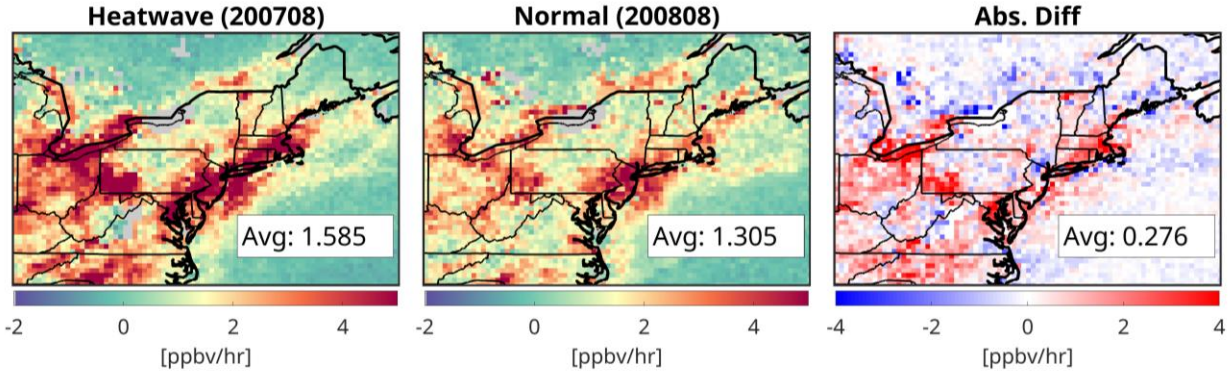

Figure S8. The maps of PO_3 within PBL in August 2007 (left), August 2008 (middle), and their absolute difference (right).

To study the reasons behind the accelerated PO_3 during this episode, we explore the respective changes in ozone precursors and the sensitivities by the heatwave. Figure S9 contrasts the differences in NO_2 and HCHO levels within the PBL region for two episodes. These maps are derived from the bias-corrected OMI VCDs scaled to the PBL region using MINDS simulations. Different wind patterns are most likely the cause of the differences in NO_2 patterns over cities; we see different shapes of NO_2 plumes over NYC, Toronto, and Boston. Additionally, we see some uniform enhancements of NO_2 in several inland regions, such as Washington DC, Philadelphia, North Carolina, Tennessee, and Ohio. While we cannot definitively locate the cause

of these enhancements without additional measurements and models, we can speculate that rising temperature can increase both nitrification and denitrification microbial activities under optimal soil moisture causing soil NO_X emissions to rise. Another possible explanation could be that NO_X reservoirs (such as PAN and alkyl nitrate) can rapidly be converted back to NO_2 because of higher temperature and more sunshine. HCHO levels are markedly high during the heatwave event in comparison to the baseline (>2 ppbv). The enhanced biogenic emissions and photochemistry are the causes.

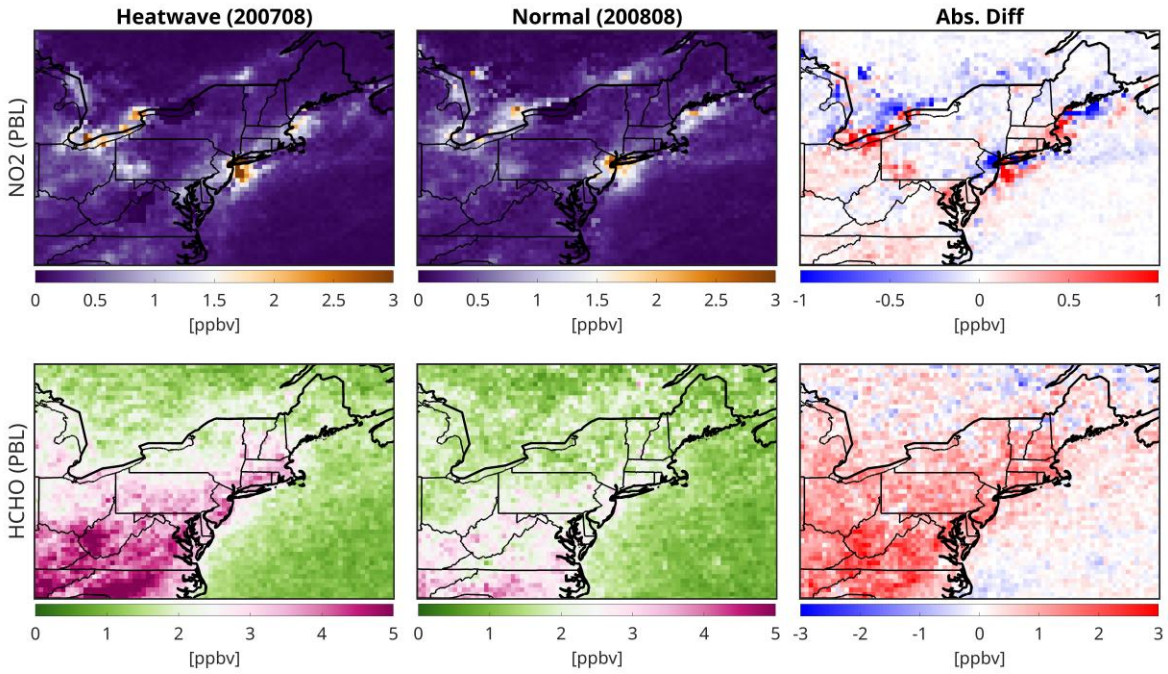

Figure S9. The maps of NO_2 (top) and HCHO (bottom) concentrations within PBL averaged in month of August in 2007 (heatwave) and 2008 (a normal condition), and their absolute differences. The abundance of HCHO and NO_2 are informed by bias-corrected OMI retrievals.

Using the spatially-varying sensitivity of PO_3 to NO_2 and HCHO provided by our product, we find that in rural and suburban areas, the derivative of PO_3 to NO_X tends to be high (NO_X-sensitive regimes) (Figure S10), indicating that even a small increase in NO_2 in several inland regions can boost the sensitivity of PO_3 to NO_2 greatly. This observation is consistent with findings from Geddes et al. (2022), who reported a similar trend of increasing ozone sensitivity to soil NO_X emissions across various remote regions in the U.S.

We observe that higher levels of HCHO significantly increase the sensitivity of PO_3 to HCHO in several high-NO_X areas, including Toronto, Boston, Washington DC, Philadelphia, and Buffalo, as illustrated in Figure S10. As noted before, the sensitivity maps are influenced by both the magnitude of a precursor and the derivative of PO_3 with respect to a precursor. In high-NO_X regions, the derivative of PO_3 to HCHO is typically large (i.e., VOC-sensitive). Consequently, elevated HCHO concentrations lead to a greater sensitivity of PO_3 to HCHO levels. Conversely, in remote regions where the derivative of PO_3 to HCHO is small, increases in HCHO cannot induce noticeable effect on PO_3. An exception to the general increase in PO_3 sensitivity to

HCHO occurs over NYC. This anomaly can be attributed to the different shape of the NO_2 plume in August 2008 as compared to 2007. In August 2007, as shown in Figure S9, NO_2 concentrations in NYC were dispersed over the ocean, resulting in less VOC-sensitive conditions (lower derivative of PO_3 to HCHO) within the city. As a result, PO_3 sensitivity values to HCHO decrease because the first-order derivative decreases.

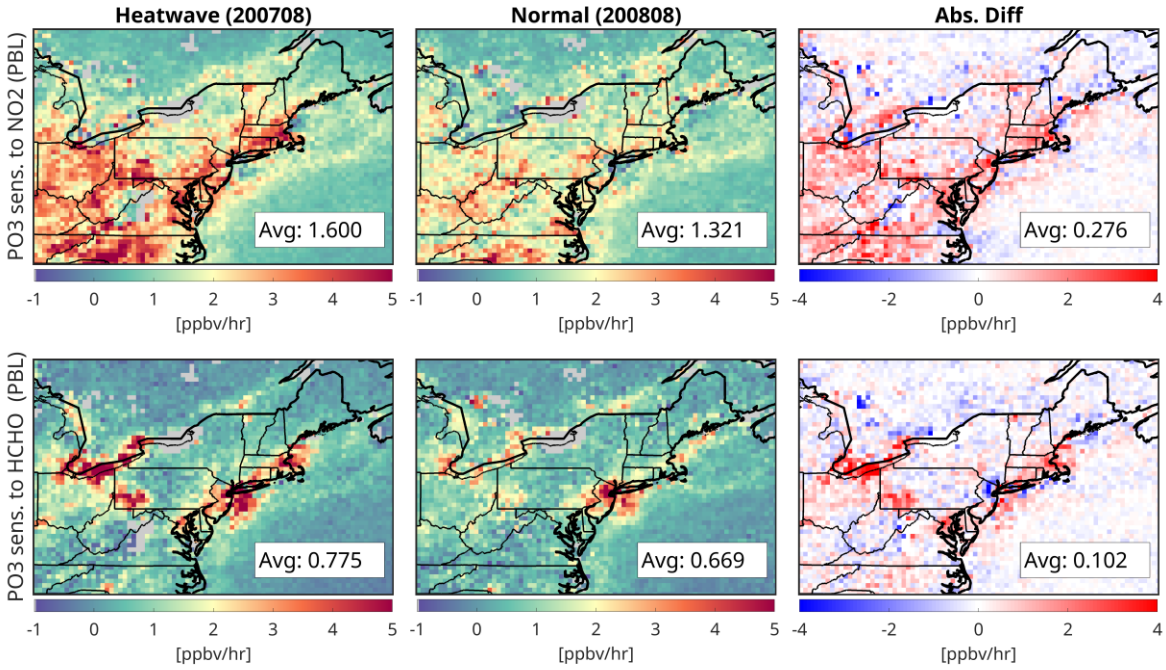

Figure S10. A similar layout as shown in Figure 8, but with the sensitivity outputs derived from the PO_3DNN algorithm.

These results suggest that the rapid calculation capabilities of our product can aid in identifying the causes behind unusual ozone exceedances triggered by weather events, without requiring substantial expertise or computational resources for fine-tuning chemical transport models. However, it is important to note that those models are essential for comprehensively understanding all physiochemical processes responsible for ozone formation and loss, as they provide explicit and process-based details.

4. References:

Demetillo, M. A. G., Anderson, J. F., Geddes, J. A., Yang, X., Najacht, E. Y., Herrera, S. A., Kabasares, K. M., Kotsakis, A. E., Lerdau, M. T., and Pusede, S. E.: Observing Severe Drought Influences on Ozone Air Pollution in California, Environ. Sci. Technol., 53, 4695–4706, https://doi.org/10.1021/acs.est.8b04852, 2019.

Duncan, B. N., Yoshida, Y., Damon, M. R., Douglass, A. R., and Witte, J. C.: Temperature dependence of factors controlling isoprene emissions, Geophys. Res. Lett., 36, https://doi.org/10.1029/2008GL037090, 2009.

Geddes, J. A., Pusede, S. E., and Wong, A. Y. H.: Changes in the Relative Importance of Biogenic Isoprene and Soil NOx Emissions on Ozone Concentrations in Nonattainment Areas of the United States, J. Geophys. Res.-Atmos., 127, e2021JD036361, https://doi.org/10.1029/2021JD036361, 2022.

Kleinman, L. I., Daum, P. H., Imre, D., Lee, Y.-N., Nunnermacker, L. J., Springston, S. R., Weinstein-Lloyd, J., and Rudolph, J.: Ozone production rate and hydrocarbon reactivity in 5 urban areas: A cause of high ozone concentration in Houston, Geophys. Res. Lett., 29, 105-1-105–4, https://doi.org/10.1029/2001GL014569, 2002.

Pusede, S. E., Steiner, A. L., and Cohen, R. C.: Temperature and Recent Trends in the Chemistry of Continental Surface Ozone, Chem. Rev., 115, 3898–3918, https://doi.org/10.1021/cr5006815, 2015.

Pyrgou, A., Hadjinicolaou, P., and Santamouris, M.: Enhanced near-surface ozone under heatwave conditions in a Mediterranean island, Sci. Rep., 8, 9191, https://doi.org/10.1038/s41598-018-27590-z, 2018.

Wu, W., Fu, T.-M., Arnold, S. R., Spracklen, D. V., Zhang, A., Tao, W., Wang, X., Hou, Y., Mo, J., Chen, J., Li, Y., Feng, X., Lin, H., Huang, Z., Zheng, J., Shen, H., Zhu, L., Wang, C., Ye, J., and Yang, X.: Temperature-Dependent Evaporative Anthropogenic VOC Emissions Significantly Exacerbate Regional Ozone Pollution, Environ. Sci. Technol., 58, 5430–5441, https://doi.org/10.1021/acs.est.3c09122, 2024.

Additional Figures:

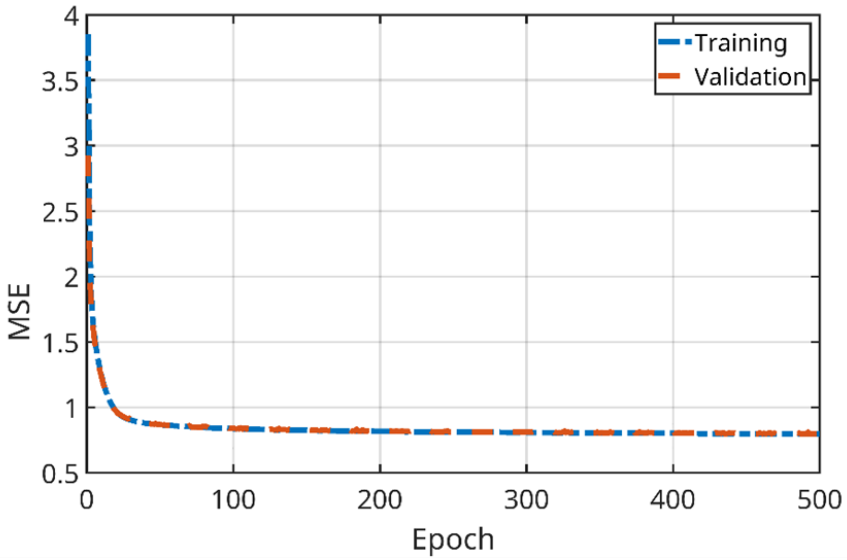

Figure S11. The learning curve shows the evolution of training and validation MSEs as a function of epochs.

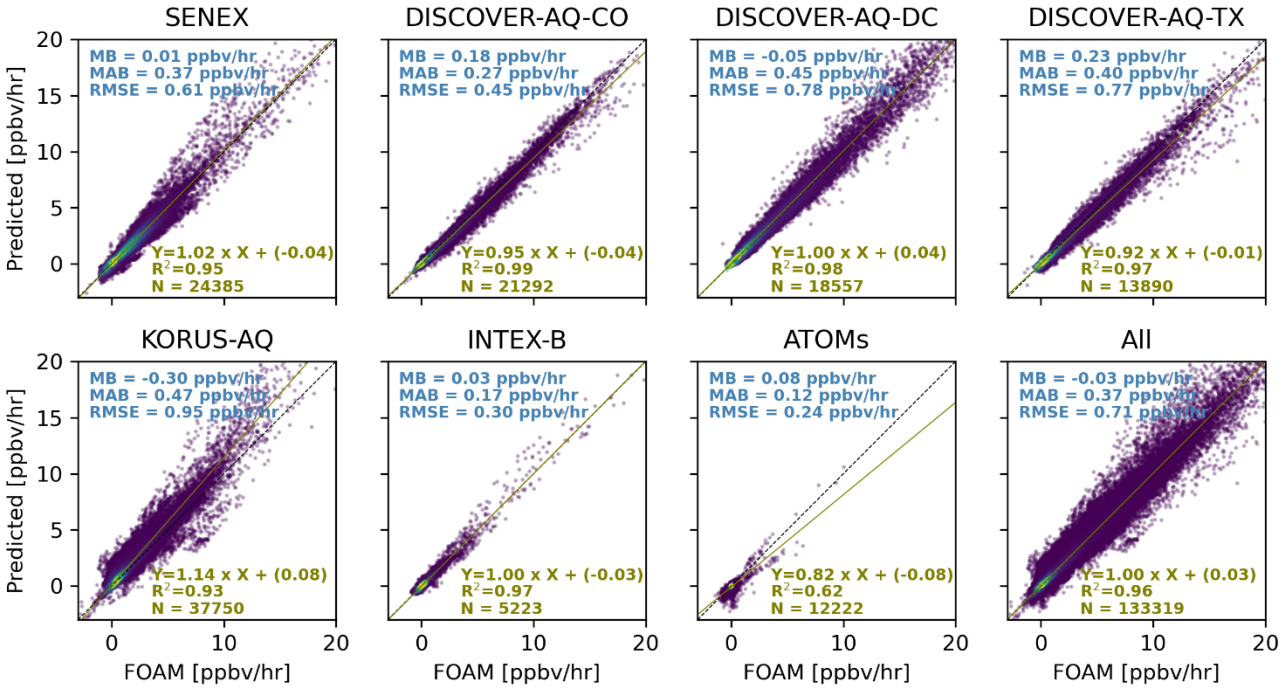

Figure S12. Scatterplots comparing observationally-constrained F0AM model PO_3 and the predictions based on the DNN for the whole data (test+validation+training) from each air quality campaign. "All" denotes all test data.

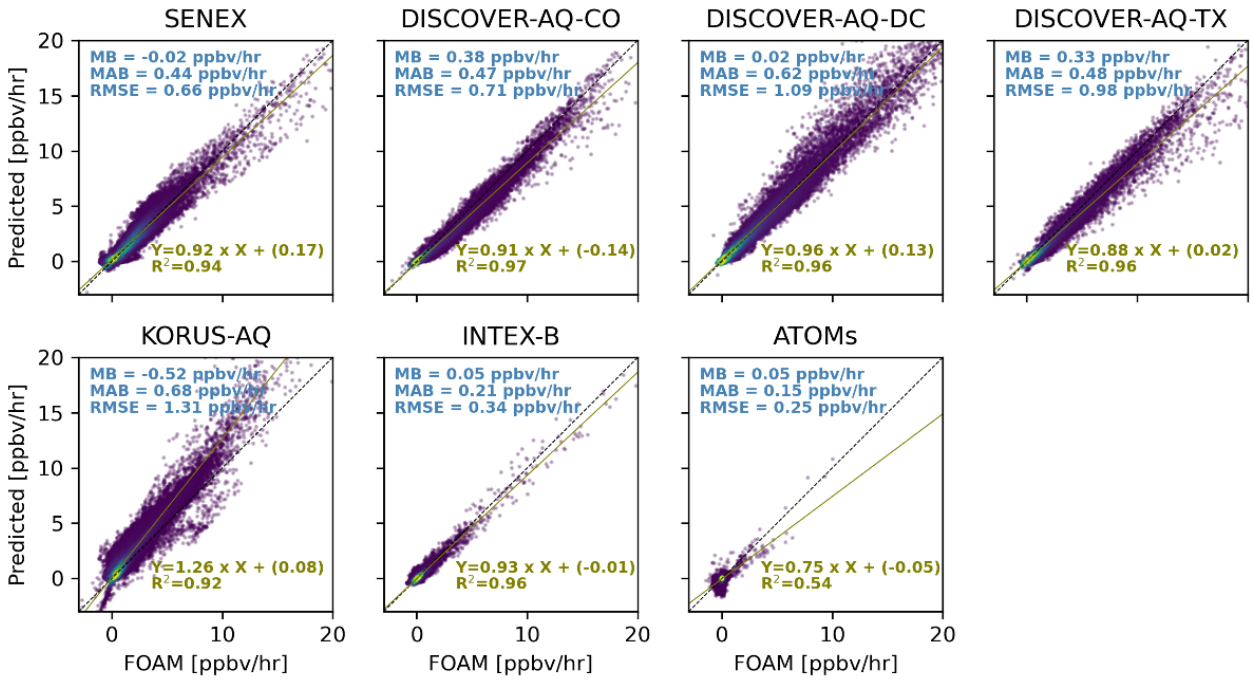

Figure S13. Scatterplots comparing observationally-constrained F0AM model PO_3 and the predictions based on dropping each campaign from the training data and using them as benchmarks.

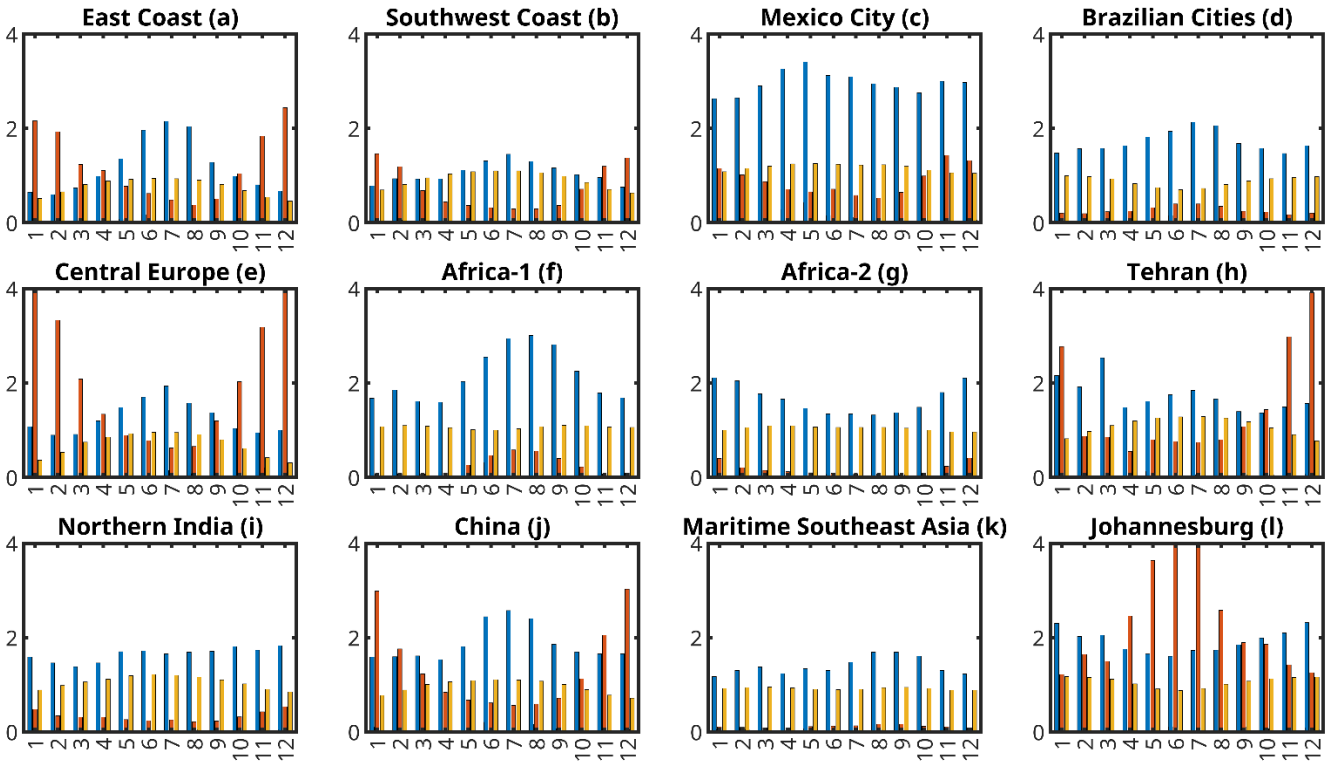

Figure S14. Absolute values of HCHO, NO_2, and jNO_2 for several regions shown in Figure 6 in the main manuscript. These data are based on 2005-2007 time period. HCHO and NO_2 units are ppbv. jNO_2 is in 1×10^{-3}/s unit.

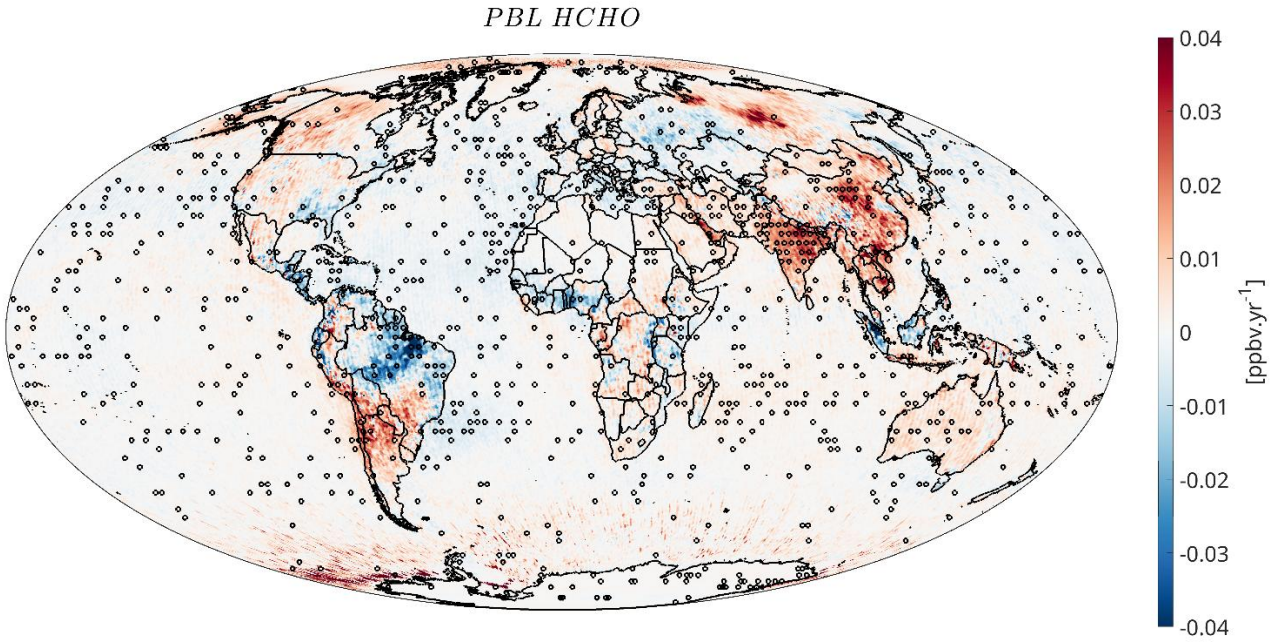

Figure S15. Linear trends of HCHO mixing ratios within the PBL derived from OMI+MINDS in 2005-2019. Dots indicate a statistically significant trend.

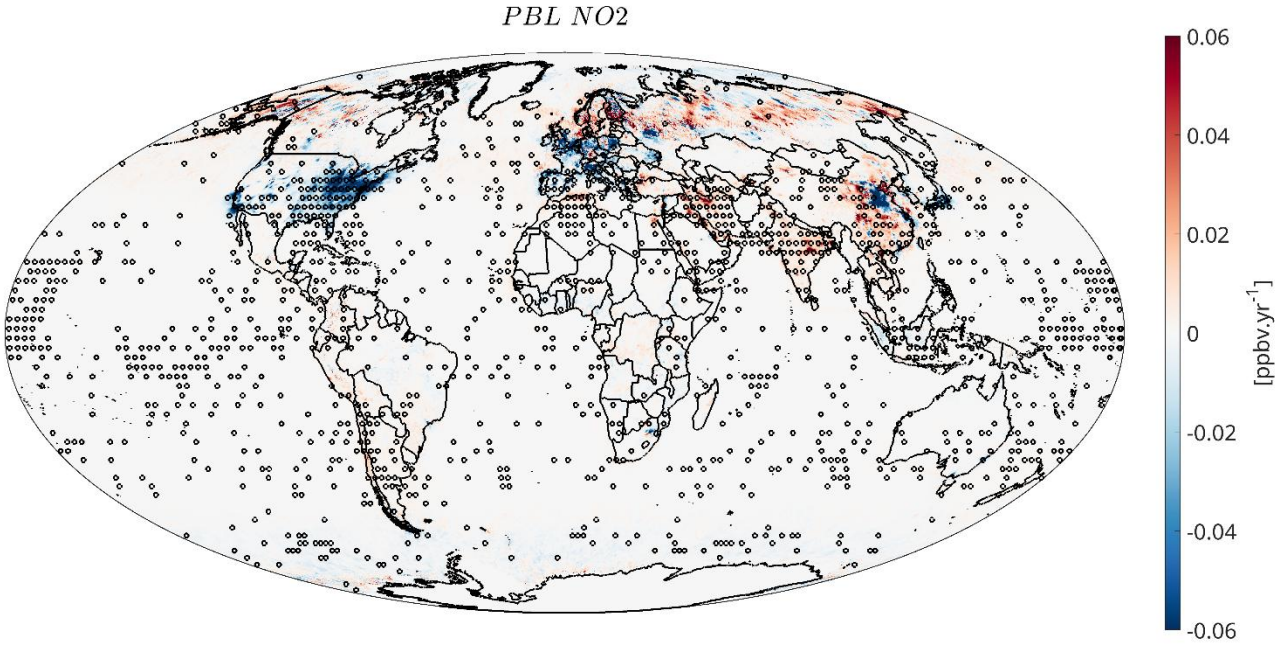

Figure S16. Linear trends of NO_2 mixing ratios within the PBL derived from OMI+MINDS in 2005-2019. Dots indicate a statistically significant trend.

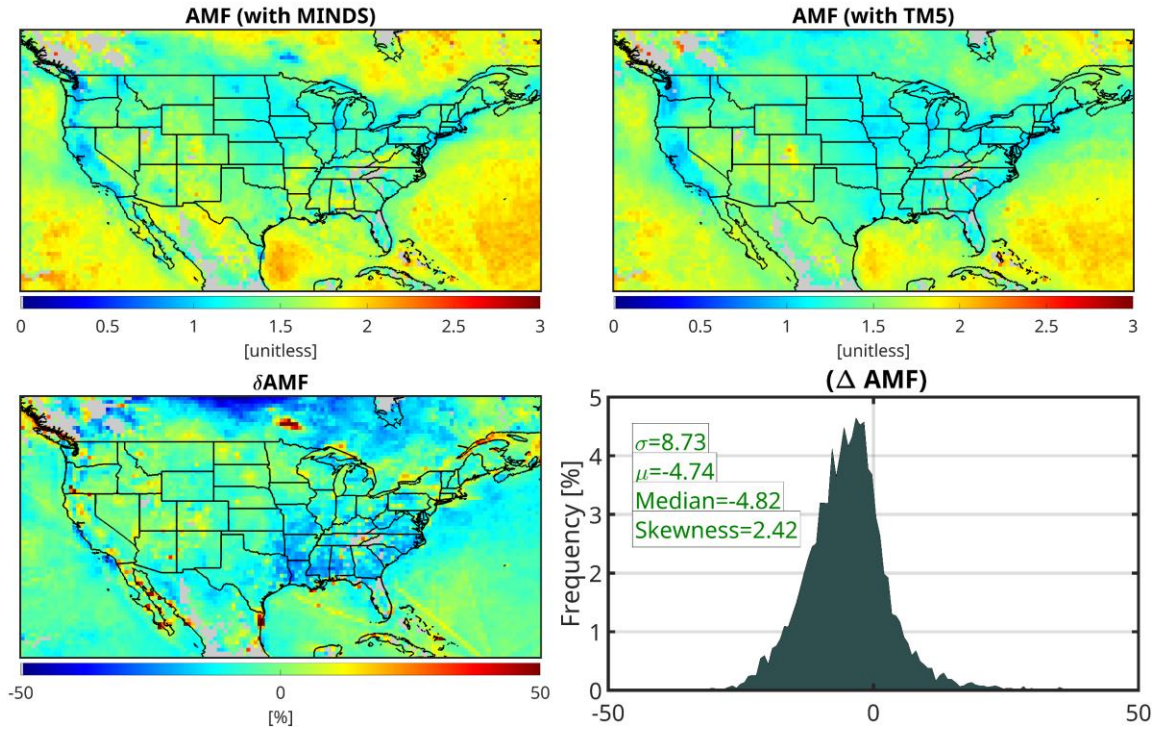

Figure S17. Recalculation of AMFs using MINDS vertical shape factors contrasted with the default profiles coming from TM5. The differences are within 20% in polluted regions with active photochemistry.

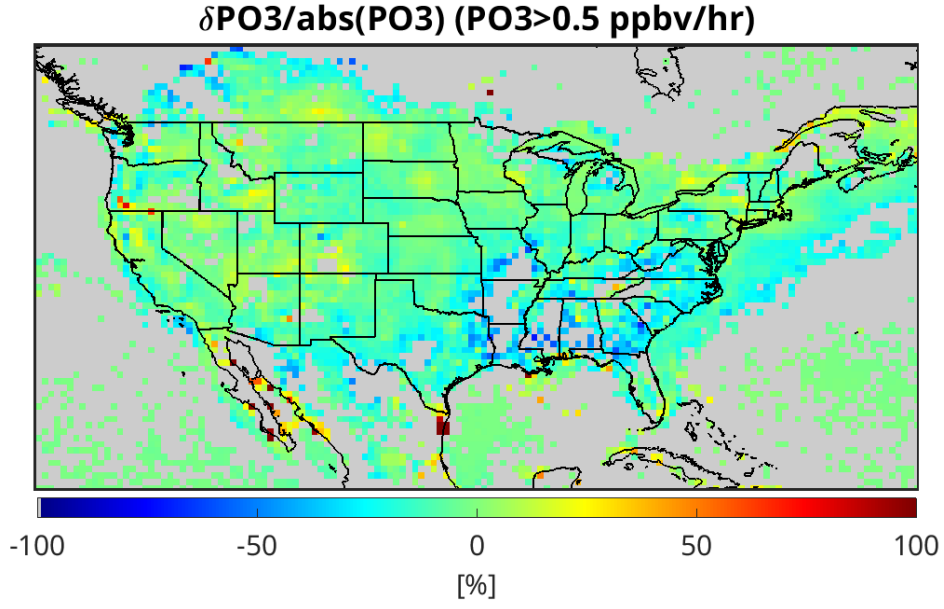

Figure S18. The impact of AMFs recalculation of TROPOMI NO_2 on relative PO_3 over regions undergoing PO_3>0.5 ppbv/hr.

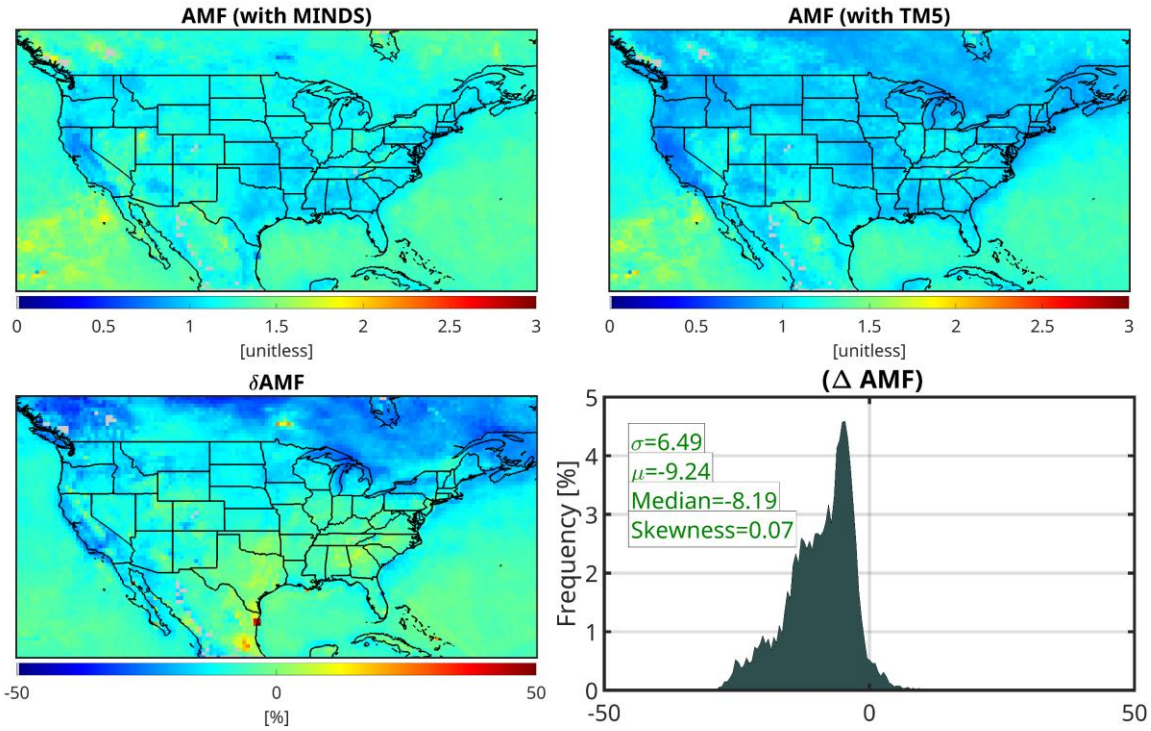

Figure S19. Same as Figure S17 but for HCHO.

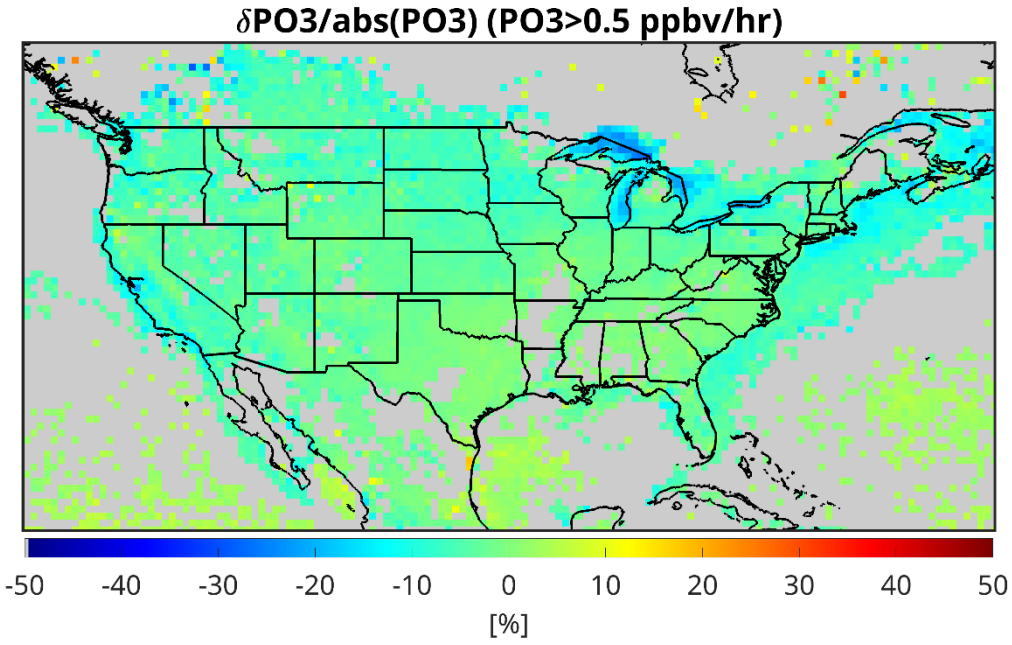

Figure S20. Same as Figure S18 but for HCHO.